BIOCHEMISTRY
including biophysical chemistry & molecular biology
Article

Biochemistry **2010,** *49,* 10553–10564 10553
DOI: 10.1021/bi1014216

Molecular Level Insights into Thermally Induced α-Chymotrypsinogen A Amyloid Aggregation Mechanism and Semiflexible Protofibril Morphology†

Aming Zhang,‡ Jacob L. Jordan,‡ Magdalena I. Ivanova,§ William F. Weiss IV,∥,⊥ Christopher J. Roberts,∥ and Erik J. Fernandez*,‡

‡*Department of Chemical Engineering, University of Virginia, Charlottesville, Virginia 22904, United States,* §*UCLA-DOE Institute for Genomics and Proteomics, Los Angeles, California 90095-1570, United States , and* ∥*Department of Chemical Engineering, University of Delaware, Newark, Delaware 19716, United States.* ⊥*Present address: Biopharmaceutical Research and Development, Lilly Research Laboratories, Eli Lilly and Co., Indianapolis, IN 46285*

Received September 2, 2010; Revised Manuscript Received November 5, 2010

ABSTRACT: Understanding nonnative protein aggregation is critical not only to a number of amyloidosis disorders but also for the development of effective and safe biopharmaceuticals. In a series of previous studies [Weiss et al. (2007) *Biophys. J. 93*, 4392−4403; Andrews et al. (2007) *Biochemistry 46*, 7558−7571; Andrews et al. (2008) *Biochemistry 47*, 2397−2403], α-chymotrypsinogen A (aCgn) and bovine granulocyte colony stimulating factor (bG-CSF) have been shown to exhibit the kinetic and morphological features of other nonnative aggregating proteins at low pH and ionic strength. In this study, we investigated the structural mechanism of aCgn aggregation. The resultant aCgn aggregates were found to be soluble and exhibited semiflexible filamentous aggregate morphology under transmission electron microscopy. In addition, the filamentous aggregates were demonstrated to possess amyloid characteristics by both Congo red binding and X-ray diffraction. Peptide level hydrogen exchange (HX) analysis suggested that a buried native β-sheet comprised of three peptide segments (39−46, 51−64, and 106−114) reorganizes into the cross-β amyloid core of aCgn aggregates and that at least ∼50% of the sequence adopts a disordered structure in the aggregates. Furthermore, the equimolar, bimodal HX labeling distribution observed for three reported peptides (65−102, 160−180, and 229−245) suggested a heterogeneous assembly of two molecular conformations in aCgn aggregates. This demonstrates that extended β-sheet interactions typical of the amyloid are sufficiently strong that a relatively small fraction of polypeptide sequence can drive formation of filamentous aggregates even under conditions favoring colloidal stability.

Nonnative protein aggregation refers to self-association into high molecular weight species that are composed of monomers with altered secondary and/or tertiary structure relative to their native counterparts. Depending on the aggregation conditions, the resulting nonnative aggregates can adopt a diversity of morphologies from amorphous particles to highly aligned amyloid fibrils (*1*−*3*). In the past three decades, the amyloid fibril class of nonnative aggregates has been most extensively studied because of their high degree of order and their relevance to human disease (*4*). More recently, accumulating evidence has also demonstrated that nonpathogenic proteins and synthetic polypeptides can form amyloids when appropriate aggregation conditions are provided (*5*, *6*). Notably, though these amyloid-forming proteins and peptides are of diverse sequence and native structure, they all form fibrils that are rich in β-sheet structure with a characteristic X-ray diffraction pattern (*7*−*12*) and the ability to bind the dyes Congo red and thioflavin T (ThT)[1] (*13*−*15*).

The presence of protein aggregates as impurities in therapeutic protein products has raised the concerns of potency reduction, adverse side effects, and/or enhanced immunogenic response (*16*−*20*). Therefore, the control and prevention of protein aggregation remain an important challenge during development of processing and formulation conditions that maximize protein product shelf life (*21*−*23*). A common strategy to increase protein stability against aggregation is to use solution conditions favorable for protein colloidal stability (e.g., characterized by the osmotic second virial coefficient B_{22}), such as low pH and ionic strength where the repulsive interaction between protein molecules is enhanced (*24*, *25*).

Previous studies suggest an interesting phenomenon that many nonrelated proteins (e.g., insulin (*26*), β-lactoglobulin (*27*), transthyretin (*28*), myoglobin (*5*), lysozyme (*29*), BSA (*30*), α-synuclein (*31*)) can form fibrillar aggregates when incubated under low ionic strength and low pH conditions that produce strong electrostatic repulsion between monomers. In contrast, these same proteins form amorphous particulates when incubated at high ionic strength and pH close to their isoelectric point (*32*). The formation of two different aggregate morphologies may be determined by the different intermolecular interactions involved: specific and extended β-sheet interactions lead to amyloid aggregates while nonspecific interactions result in amorphous,

†This research work was funded by financial support from Amgen, Inc.

*Corresponding author: 434-924-1351 (phone); 434-982-2658 (fax); erik@virginia.edu (e-mail).

[1]Abbreviations: aCgn, α-chymotrypsinogen A; bG-CSF, bovine granulocyte colony stimulating factor; ThT, thioflavin T; HX-MS, hydrogen exchange mass spectrometry; DLS, dynamic light scattering; FT-IR, Fourier transform infrared spectroscopy.

Published on Web 11/10/2010

disordered aggregates. High colloidal stability appears to prevent nonspecific molecular association, allowing β-sheet interactions to facilitate amyloid fibril formation (*5*, *33*).

However, several questions remain for the amyloid formation of globular proteins. First, which regions in a full-length protein contribute to the cross-β amyloid pattern in the resulting fibrils? Second, what structural reorganization is necessary to form extended β-sheets typical for amyloid from the native structure? Third, how do these extended β-sheet interactions contribute to the various morphologies of amyloid fibrils when considerable disordered structure is also present in protein aggregates? To address the first question, both experimental measurement and computational prediction of amyloid-forming regions have been developed and performed for multiple well-known amyloid formation proteins (*34*−*37*). However, correlation of these two approaches has been less attempted, particularly for full-length proteins. For the second and third questions, few proteins have been studied at the molecular level to relate structural reorganization to the adopted amyloid morphology due to the difficulty in characterizing the complex structures formed (*10*, *34*, *38*).

In a recent series of publications, the nonnative aggregation kinetics of two model proteins, bovine granulocyte colony stimulating factor (bG-CSF) and α-chymotrypsinogen A (aCgn), at low pH and low ionic strength were extensively investigated (*16*, *39*, *40*). The formed soluble aggregates from both proteins showed indistinguishable semiflexible filamentous morphologies under transmission electron microscopy (TEM), similar to precursor protofibrils of many well-characterized amyloid fibrils (*41*−*43*). In addition, both filamentous aggregates had increased β-sheet content relative to their native states and bound the dye thioflavin T (ThT) (*16*), suggesting that the nonnative aggregates of bG-CSF and aCgn may be amyloid-like. Because human G-CSF is used as a pharmaceutical protein, the formation of protofibrillar aggregates potentially raises concerns about immunogenicity (*18*, *19*) and even potential cytotoxicity by analogy to protein amyloid aggregates associated with neurodegenerative disease (*44*, *45*).

In this study, we analyze the molecular level structural reorganization during the aggregation of aCgn at low pH and ionic strength. First, we demonstrate aCgn filamentous aggregates exhibit Congo red binding and X-ray diffraction patterns characteristic of amyloids. Second, comparison of native monomer and filamentous aggregates by hydrogen exchange detected by mass spectrometry (HX-MS) reveals a detailed picture of local structural rearrangement upon aCgn amyloid formation. In this process, aCgn molecule undergoes substantial structural unfolding, and many residues are excluded from the core of the amyloid. In contrast, three short segments gain high solvent protection after aggregation, suggesting they form extended β-sheets characteristic for amyloids. Further, these HX-protected segments align with computationally predicted aggregation hotspots, i.e., regions with high propensity to form extended β-sheets. Using the structural constraints from the measurements, a prospective model of the monomer structure within the amyloid was constructed, which helps to explain the interactions involved during aggregation under colloidally stable conditions.

MATERIALS AND METHODS

Materials. aCgn (6× crystallized and lyophilized powder, catalog no. C4879) was purchased from Sigma-Aldrich. Deuterium oxide (D_2O) was obtained from Cambridge Isotope Laboratories (99.9% deuterium; Andover, MA). An immobilized pepsin (from porcine gastric mucosa, catalog no. 6887; Sigma) column for online proteolysis was prepared as previously described (*38*). All other reagents were purchased from Sigma unless otherwise specified.

Aggregate Sample Preparation. aCgn powder was dissolved in 10 mM citric acid buffer, pH 3.5, at a final protein concentration of 8 mg/mL. Fresh monomer samples were used immediately after dissolution in citric acid buffer. Soluble aggregates were prepared by incubating a borosilicate glass vial containing 2 mL of aCgn solution for 2.5 min at 65 °C using a circulating water bath. The 2.5 min incubation time was chosen as approximately 4−5 half-lives of monomer loss under identical aggregation condition to ensure full conversion of monomer, based on aggregation kinetics determined previously (*16*, *39*). Aggregated samples were then quenched by immediately transferring vials to an ice−water bath for another 2 min. The concentration (mass basis) of both monomer and aggregate samples was confirmed by SEC before use.

Congo Red Binding Assay. Congo red solution (120 μM in PBS buffer) was filtered through a 0.22 μm syringe filter three times before use and then mixed with 8 mg/mL aCgn samples in a 96-well plate. After an incubation and binding period of 45 min at room temperature, absorbance at wavelengths of 405 and 540 nm was measured using a SpectraMax Plus^{384} microplate reader (Molecular Devices, Sunnyvale, CA). PBS buffer was used as the blank reference. The concentration of Congo red (mol/L) bound to aCgn was determined as described by Klunk et al. (*13*).

Fourier Transform Infrared Spectroscopy (*FT-IR*). Three hundred microliters of 8 mg/mL aCgn aggregate sample was spread on a ZnSe plate and dried under gentle flow of dry air at room temperature. The infrared spectrum was recorded on a Bio-Rad FTS-60A spectrometer equipped with a Harrick Praying Mantis diffuse reflectance accessory. The spectrum was obtained from 100 averaged scans recorded at a resolution of 2 cm^{-1} in the range of protein amide I absorption (1580−1720 cm^{-1}). Spectra of native aCgn were obtained from aCgn monomer solution dissolved in D_2O-based buffer with identical parameter settings. Spectral deconvolution was performed using Origin software with multiple Gaussian peak fitting.

Transmission Electron Microscopy (*TEM*). Thermally induced aCgn aggregates (8 mg/mL) were dialyzed against 2 mM citrate, pH 3.5. Negatively stained specimens for transmission electron microscopy (TEM) were prepared by applying 5 μL of sample on hydrophilic 400 mesh carbon-coated Formvar support films mounted on copper grids (Ted Pella, Inc.). The samples were allowed to adhere for 3 min, rinsed twice with distilled water, and stained for 1 min with 1% uranyl acetate (Ted Pella, Inc.). Grids were examined in a CM-120 (FEI) microscope.

X-ray Diffraction of aCgn Filamentous Aggregates. aCgn aggregate samples were first dialyzed against 2 mM sodium citrate, pH 3.5, to remove the salts. Oriented samples for fiber diffraction were prepared by placing 4 μL of aCgn aggregates between two fire-polished, silanized glass capillaries that were spaced 1 mm apart. After 30 min, a second 4 μL drop of aggregates was added. This was repeated three more times, and then the samples were air-dried. X-ray diffraction data of the oriented samples were collected on beamline 24-ID-E at the Advanced Photon Source (APS) at Argonne National Laboratory. The sample-to-film distance was 500 mm. Data were collected on a Quantum315 detector using an X-ray beam wavelength of 0.97918 Å.

Hydrogen/Deuterium Exchange. The procedure shown schematically in Figure 1 was used to carry out HX analysis.

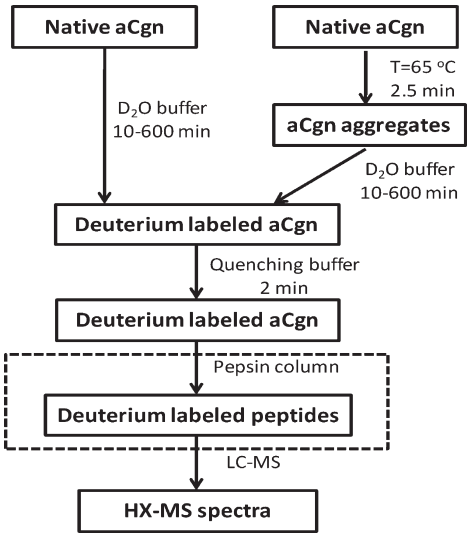

FIGURE 1: HX procedure used to measure deuterium labeling of native aCgn and thermally induced aggregates at both intact molecule and peptide level. The experimental step in dotted box is performed only during peptide level HX analysis.

Whole protein H/D exchange of aCgn monomer and thermally induced aggregates was initiated by diluting 5 μL of aCgn solution into 45 μL of citric acid buffer, made up in D_2O at pH 3.5. The labeling was carried out at room temperature for durations from 10 s to 600 min and then quenched by adding 150 μL of cold 8 M guanidine hydrochloride solution and 20 μL of 1 M tris-(2-carboxyethyl)phosphine (TCEP) solution (both at pH 3.0). The formed aCgn aggregates were highly stable (*46*), and a high concentration of guanidine hydrochloride (6 M in quenched sample) was required to dissociate aggregates back to monomer in a short time (2 min at ice cold) for mass analysis. The quenched aCgn sample was desalted with a peptide trapping column (1 mm i.d. × 8 mm, catalog no. TR1/25108/01; Michrom Bioresources, Auburn, CA) before delivery to a standard ESI ion-trap mass spectrometer (LTQ; Thermo Electron Corp., San Jose, CA) for analysis. A short gradient of acetonitrile (ACN) from 5% to 80% in 5 min (50 μL/min delivered by Surveyor MS Pump, Thermo, San Jose, CA) was used to elute intact aCgn from the trapping column.

For peptide level H/D exchange experiments, a high concentration of guanidine hydrochloride used to dissociate aggregates would be detrimental to pepsin activity. Therefore, after aggregate dissolution, the quenched aCgn sample was diluted 5-fold with 10 mM citric acid buffer, pH 3.0. The digestion was achieved by flowing aCgn samples through an online immobilized pepsin column. The resultant peptides were desalted with the same peptide trapping column and then separated in a second, resolving column (Vydac C_{18}, 0.3 × 50 mm; Grace Vydac, Hesperia, CA). In peptide separation, a longer ACN gradient elution (from 15% to 40% over 15 min) was used. All of the reporter peptides used for local structural analysis were assigned by performing MS/MS mass spectrometry, followed by analysis with TurboSEQUEST software. To minimize artifactual exchange during the analysis time, all of the columns, loops, and lines were immersed in an ice bath during all of the experiments.

The deuteration level for intact molecule and each reporter peptide was calculated by the equation:

$$D\% = \frac{m - m_0}{(m_{100} - m_0) \times 0.9} \times 100 \quad (1)$$

where m is the measured centroid mass of the deuterated molecule or peptide after a particular labeling time; m_0 and m_{100} are the two centroid mass limits of a molecule and reporter peptide from zero-deuteration and full-deuteration control experiments, respectively. The factor of 0.9 in the denominator accounts for the 90% deuterium in the labeling solution.

Dynamic Light Scattering. The size distribution and polydispersity of aCgn aggregates formed at different incubation times were measured by dynamic light scattering. Experiments were performed at 25 °C with a DynaPro plate reader (Wyatt Technology, Santa Barbara, CA). The scattering angle was 90°. All of the samples were diluted to 0.5 mg/mL and filtered through a 0.22 μm syringe driven filter before each measurement. Scattered light intensity of aCgn aggregate samples was averaged over a 5 s period to obtain autocorrelation functions in the manufacturer's software, DYNAMICS (Wyatt Technology, Santa Barbara, CA). Twenty acquisitions were performed as one measurement, and three measurements were made for each aggregate sample. In data analysis, aggregate size distribution and polydispersity were determined using a regularization method.

Model Construction of Amyloid aCgn Aggregates. Structural modeling of aCgn aggregates was based on all of the information obtained from X-ray fibril diffraction, FT-IR, and peptide level HX analysis. The model building was performed with the graphics program O (*47*) and COOT (*48*). This crude model was then energy minimized with the program CNS by optimizing hydrogen bonding and removing steric clashes (*49*). For more information about the model construction, see the Supporting Information.

RESULTS

Amyloid Structure in Thermally Induced aCgn Aggregates. The kinetics of aCgn nonnative aggregation under elevated temperature and a range of pH and [NaCl] has been previously investigated using SEC and multiangle light scattering (*1*, *16*, *39*, *50*). Low pH, low ionic strength, thermally induced aCgn aggregates appear to be linear, semiflexible filaments (shown in Figure 2A). These resemble the intermediate protofibrils of many amyloid fibrils. However, aCgn filamentous aggregates under this solution condition do not aggregate appreciably with each other (*1*, *46*, *50*), unlike many amyloid-forming proteins (*51*, *52*). Thermally induced aCgn aggregates exhibit increased β-sheet content and ThT binding, indicating the prospect of amyloid structure in thermally induced aCgn aggregates. But the above evidence was not conclusive because nonamyloid aggregates were also found to display each of these characteristics (*53*, *54*).

To determine more conclusively whether aCgn aggregates possess amyloid structure, we further characterized them by Congo red binding and X-ray diffraction. As shown in Figure 2B, filamentous aggregates bind considerably more Congo red than native aCgn. Consistent with this, the oriented samples of aCgn aggregates (Figure 2C) had the characteristic for amyloid cross-β X-ray diffraction pattern (*15*). From this diffraction pattern, it can be inferred that aCgn aggregates are formed of extended β-sheets, in which β-strands are spaced 4.6 Å apart and are oriented perpendicularly to the fibril axis. The extended β-sheets are oriented parallel to the fibril axis with a sheet-to-sheet distance of ~9.5 Å.

Antiparallel β-Sheet Orientation Suggested by FT-IR Analysis. To obtain more information about the structural content of aCgn aggregates, FT-IR was performed for both

native monomer and air-dried aggregates prepared as described previously (*55*). Shown in Figure 3, the filled squares represent the experimental FT-IR data collected as described in Materials and Methods. The solid line is a fitted curve using multiple Gaussian peaks based on bandwidth deconvolution. The dotted lines are deconvoluted contributions from different secondary structure elements. β-Sheet structure as indicated by the major absorption at 1627 cm^{-1} was slightly increased in aCgn aggregates relative to native monomer. Notably, in addition to the strong absorption band at 1627 cm^{-1}, a small but significant absorption band at 1690 cm^{-1} was observed for both native monomer and aggregates. According to previous studies (*55*, *56*), the simultaneous presence of these two IR absorption peaks can be indicative of antiparallel β-sheet. Thus, the FT-IR spectra in Figure 3 suggest that aCgn β-sheets are antiparallel not only in the native monomer but also in the thermally induced aggregates.

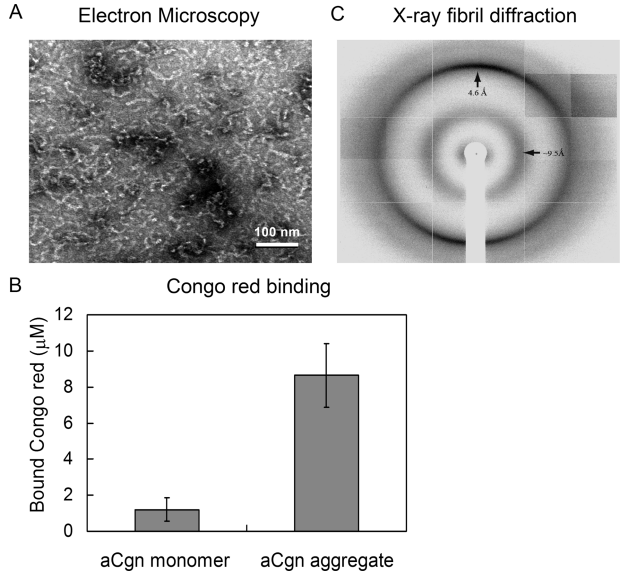

FIGURE 2: Electron microscopy (A), Congo red binding assay (B), and cross-β X-ray pattern (C) of oriented thermally induced aCgn fibrillar aggregates. In panel B, on the meridian there is a strong 4.6 Å reflection which corresponds to the distance between the β-strands. The diffuse 9.5 Å reflection corresponds to the distance between the sheets, which are oriented parallel to the fibril axis. In panel C, the error bars represent the standard deviation determined from three replicates.

Global Solvent Accessibility of aCgn Aggregates Revealed by Hydrogen Exchange. Hydrogen exchange (HX) of intact aCgn was first used to compare the overall solvent accessibility for native monomer and filamentous aggregates. Figure 4A shows the resulting mass spectra of native monomer, thermally induced aggregates, and fully unfolded monomer subjected to deuterium exchange for durations ranging from 5 to 600 min. As a denatured control, fully unfolded aCgn was prepared by dissolving protein in 6 M guanidine hydrochloride solution. Figure 4B shows the quantitative level of deuterium labeling as a function of exchange time calculated by eq 1 in Materials and Methods. As expected, fully unfolded aCgn had the highest degree of deuterium labeling among the three protein forms due to the loss of folded structure brought about by the denaturant. Under these conditions, labeling was essentially complete within 35 min. By contrast, both native monomer and aCgn aggregates were only partially labeled even after 600 min, indicating the presence of some solvent-protected structure in both states. The aggregated state of aCgn showed a much higher degree of deuterium labeling than native monomer (~80% vs 40%) at long labeling time. This suggests that in forming filamentous aggregates aCgn loses native structure to expose numerous residues to the solvent. This was consistent with the fact that the temperature used to prepare the aggregates was approximately 5−6 °C above the melting temperature (*39*). However, it is also clear from Figure 4B that the formed aggregates were not fully unstructured. Solvent-protected structure existed at least in some regions of the molecule.

Local Structural Changes Revealed by Peptide Level HX Analysis. To identify the local structural differences between native monomer and filamentous aggregates, peptide level HX analysis was carried out by incorporating an online proteolysis step. This allowed cleavage of the deuterium-labeled aCgn molecule into short reporter peptides, which retained the local deuterium labeling information. Using this approach, we identified 21 reporter peptides as described in Materials and Methods. These reporter peptides covered about 83% of the aCgn sequence, with the gaps in sequence coverage being in the Cys-rich C-terminal region.

In comparing peptide level HX between aCgn monomer and aggregates, reporter peptides from different regions of molecule showed distinct local HX patterns, suggesting aCgn transformed its local structure differently during the aggregation process.

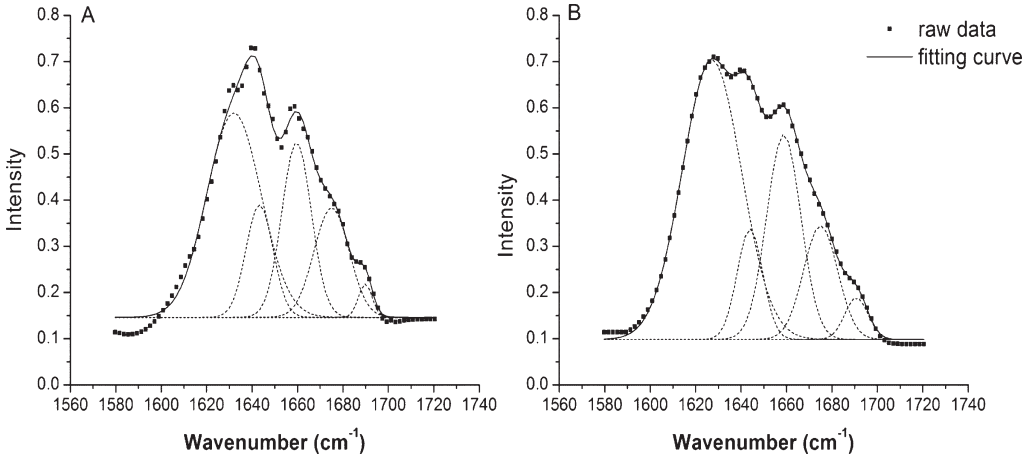

FIGURE 3: FT-IR spectra of aCgn native monomer (A) and aggregates (B). The filled squares are experimental data. The solid line is the curve derived from multiple Gaussian peak fitting, and the dotted lines represent the deconvoluted contributions from β-sheet, random coil, α-helix, β-turn, and β-sheet (peak from left to right).

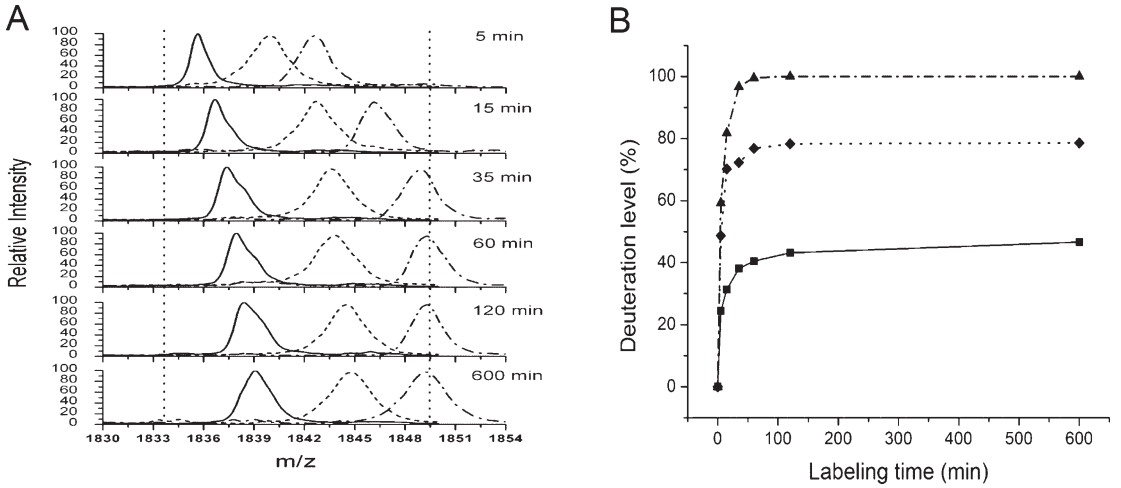

FIGURE 4: Intact protein H/D exchange analysis for aCgn. (A) Mass spectra of native monomer (solid line), thermally induced aggregates (dotted line), and fully unfolded monomer in 6 M GuanHCl (dash-dot line) with a period of exchange times. The two vertical dotted lines represent the molecular mass of unlabeled and fully labeled aCgn, respectively, for the +14 charge state. (B) The deuterium labeling profile with exchange time determined by eq 1 for native monomer (solid line), aggregates (dotted line), and fully unfolded monomer (dash-dot line).

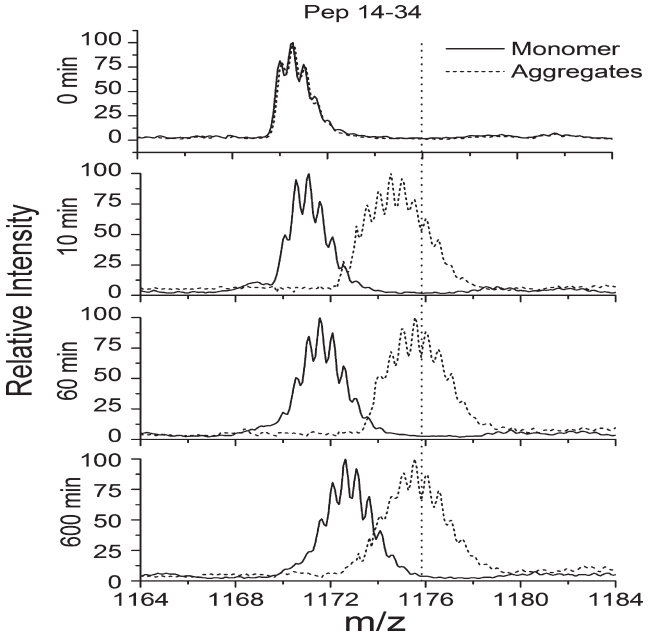

FIGURE 5: Mass spectra of peptide 14−34 representing the group of reporter peptides with increased deuterium labeling upon thermally induced aggregation. The solid curve represents labeling in the native monomer, and the dotted curve represents labeling in the aggregates. The vertical dotted line represents the maximum centroid mass from the fully labeled control. This reporter peptide has a charge state of +2. This allows the isotope distribution to be resolved, resulting in the multiple peaks observed.

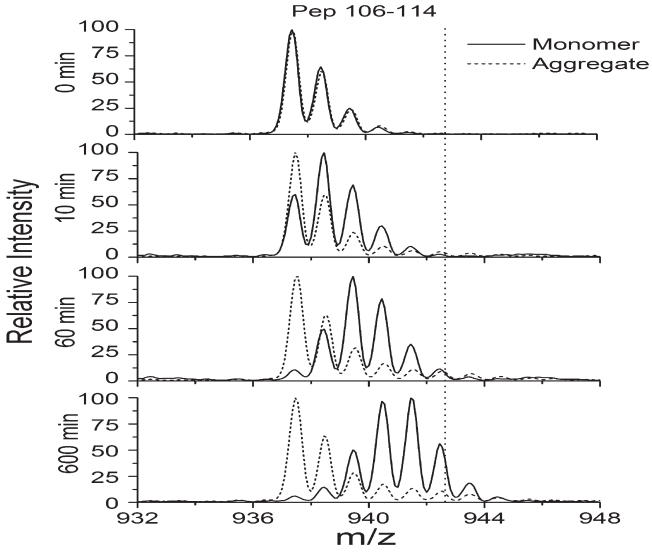

FIGURE 6: Mass spectra of reporter peptide 106−114 representing the group of reporter peptides with decreased deuterium labeling upon thermal induced aggregation. The solid curve represents labeling observed in native monomer, and the dotted curve represents labeling observed in aggregates. The vertical dotted line represents the maximum centroid mass from fully labeled control. This reporter peptide has a charge state of +1. This allows the isotope distribution to be resolved, resulting in the multiple peaks observed.

Based on the observed changes in local deuterium labeling (relative to folded monomer), the 21 reporter peptides were categorized into three groups: more solvent exposed, less solvent exposed, and bimodal.

Figure 5 shows the HX mass spectra of representative reporter peptide 14−34 from the first group. This reporter peptide behaved very similarly to intact aCgn, exhibiting an increased degree of deuterium labeling in the aggregated state compared to the native state. After 10 min, the labeling of reporter peptide 14−34 in the aggregates was already close to that of the fully unfolded control. The highly increased deuterium labeling suggested that region 14−34 of aCgn molecule became completely solvent exposed in the aggregate. In total, 10 reporter peptides were identified that all had HX behavior similar to that of peptide 14−34, and these reporter peptides constituted approximately 50% of the covered aCgn sequence (see Figure 8).

Conversely, the second group of reporter peptides, which included three peptides 39−46, 51−64, and 106−114, all showed significantly less deuterium labeling in the aggregates relative to native monomer. Results for the representative reporter peptide 106−114 are shown in Figure 6. Native monomer incorporated deuterium into this reporter peptide continuously through 600 min, while the aggregates became extremely protected from deuterium labeling in the same region to the degree that no apparent mass increase was observed over time. Such a marked reduction in solvent accessibility associated with aCgn aggregates is perhaps surprising. Normally, hydrogen exchange experiments

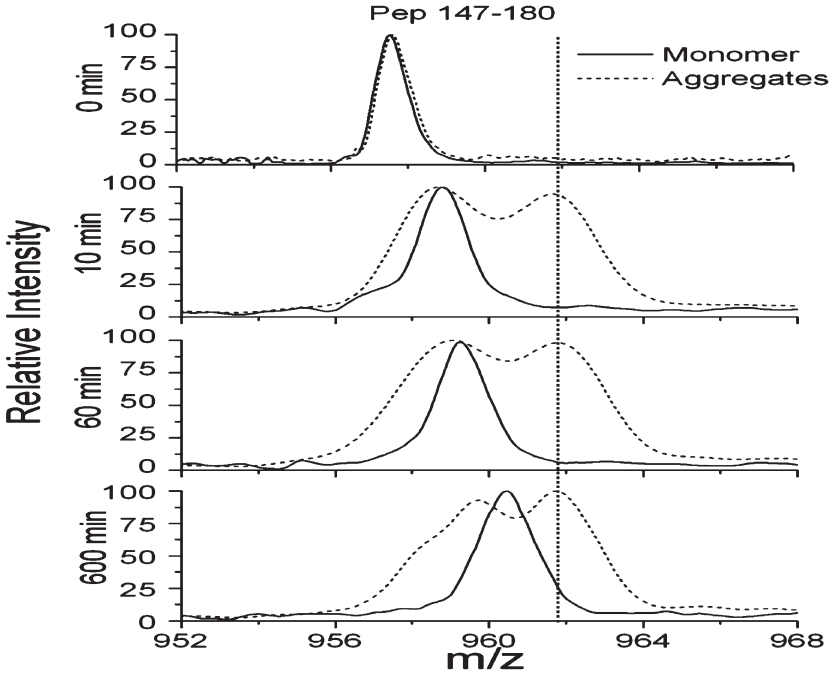

FIGURE 7: Mass spectra of peptide 147−180 representing the group of reporter peptides with bimodal HX distribution in thermally induced aggregates. The solid curve represents the labeling observed in native monomer, and the dotted curve was obtained from aggregates. The vertical dotted line represents the maximum centroid mass from the fully labeled control.

exploit the fact that the native state is more solvent protected than partially or completely unfolded states of interest. This allows unfolding rates or unfolding free energies to be determined under EX1 or EX2 isotope exchange kinetic regimes, respectively (*57*). However, exceptions to this behavior include proteins that become more ordered upon ligand binding (*58*) or proteins that form amyloid (*34*, *38*). Since aCgn aggregates were shown to have the characteristic properties of amyloid fibrils by TEM, Congo red binding, and X-ray diffraction as described above, the existence of this second group of highly protected peptides suggests that they may adopt extended β-sheet conformation typical for amyloids.

Notably, a third large group of reporter peptides was observed in which HX exhibited a bimodal labeling distribution for aCgn aggregates. As a representative, the mass spectra of reporter peptide 147−180 are shown in Figure 7. In contrast to native monomer which effectively has a single peak that shifts mass position over the labeling time, the reporter peptide from aCgn aggregates shows two resolved mass peaks. The high mass peak was fully deuterated within 10 min, while the low mass peak was partially labeled and gradually incorporated more deuterium with increased labeling time. The bimodal HX distribution indicates two molecule conformations with different local solvent accessibility are present in aCgn aggregates. In total, 8 reporter peptides exhibited this bimodal behavior, with 5 of them overlapping within region 65−102. Bimodal HX distributions have been previously reported at the peptide level for other amyloid fibrils such as α-synuclein (*34*).

Figure 8 presents all of the three groups of reporter peptides highlighted below aCgn sequence (Figure 8A) and on crystal structure (Figure 8B). Together, they show a map of aCgn local structural changes in the thermally induced aggregation process. Red bars and ribbons in panels A and B show the first group of reporter peptides with increased local solvent accessibility upon aggregation, blue for the group with decreased solvent accessibility, and yellow for group with bimodal HX distribution. The secondary structure of the aCgn native state (*59*) is also indicated in Figure 8A with a straight line (coiled structure), arrow (β-strand), and cylinder (α-helix) above the sequence. It is interesting to note that the three reporter peptides (39−46, 51−64, and 106−114) exhibiting high solvent protection in aggregates are all derived from β-strands from a buried β-sheet in the native structure in Figure 8B. This indicates that native β-sheet buried in aCgn monomer structure may rearrange into a solvent-protected structure in amyloid formation. Three reporter peptides exhibiting bimodal behavior (65−102, 160−180, and 229−245) show no correlation with native secondary structure, but they are adjacent to the buried native β-sheet, almost "sandwiching" it. The reporter peptides showing increased solvent accessibility in aggregates (highlighted in red) are mainly coiled-coil conformation in native aCgn (Figure 8B).

The bimodal HX distribution observed in the set of reporter peptides suggests that a mixture of two distinct molecule conformations with local solvent accessibility difference is present in aCgn aggregates. There are at least two possibilities that could lead to the observation of bimodal HX distributions in amyloid aggregates. First, the thermally induced aCgn aggregate samples might be a mixture of more than one type of aggregate, each being made purely of one monomer conformation. The second possibility is that there is only one aggregate species in the sample, but the aggregates consist of monomers that have adopted one of two distinct molecular conformations.

To help to distinguish these two possibilities, we extended the thermal aggregation time at 65 °C from 2.5 min to 5 and 15 min. According to previous studies (*16*), the aggregation process after 2.5 min (four to five times the half-life of monomer loss) would be dominated by aggregate−aggregate condensation due to the depletion of monomer. Analysis of aggregate size and polydispersity by DLS further confirmed this. As shown in Figure 9, after 2.5 min, the monomer peak disappeared, and the aggregate species increased both their size and polydispersity over incubation time.

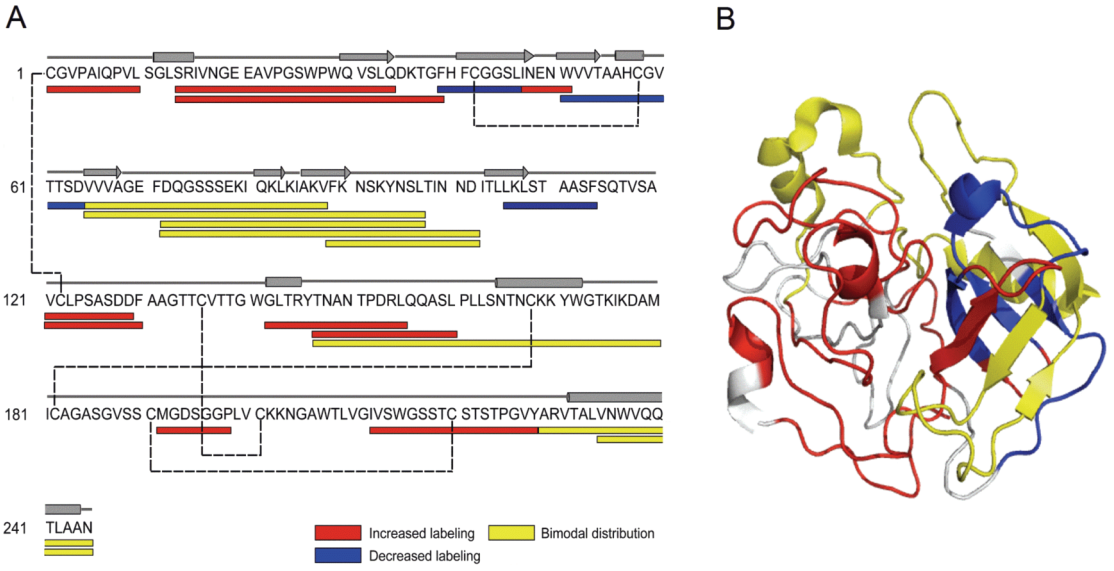

FIGURE 8: The peptide level HX behavior mapped onto the aCgn primary sequence (A) and crystal structure (PDB ID 2CGA) (B). Segments with increased deuterium labeling in aCgn aggregates are colored in red, segments with decreased deuterium labeling in blue, and segments exhibiting bimodal distributions in yellow. In panel A, the straight line, arrow, and cylinder above the sequence represent coil, β-strand, and α-helical secondary structure assigned based on the PDB structure. The dotted lines connecting two Cys residues are the five disulfide bonds in native aCgn.

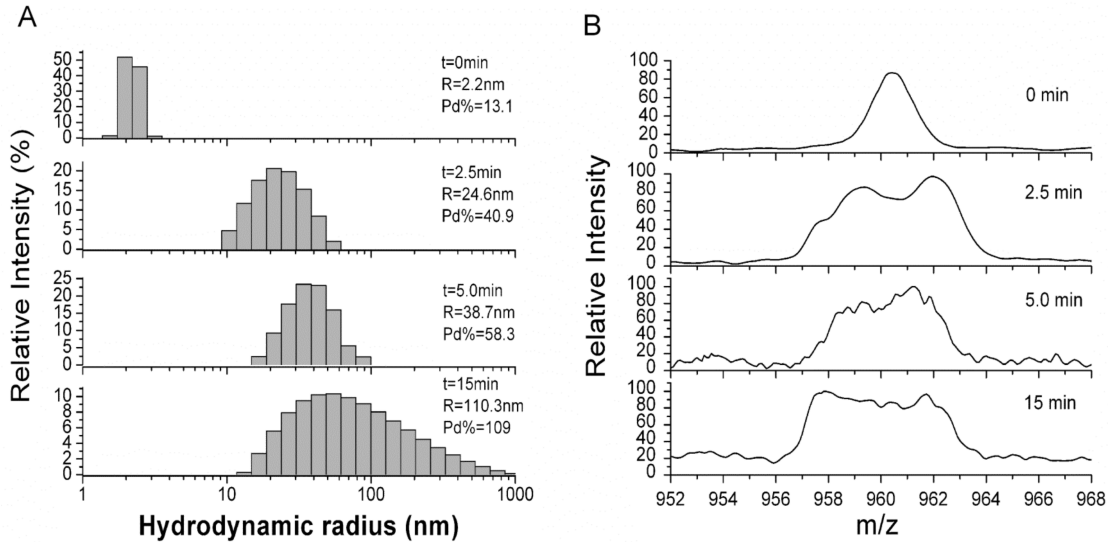

FIGURE 9: Parallel analysis of aCgn aggregates resulting from extended aggregation at 65 °C by DLS (A) and H/D exchange (B). The aggregation time, average aggregate size, and polydispersity (Pd%) are labeled in each panel for DLS measurement. Panel B shows the bimodal H/D distribution for reporter peptide 147−180 from three corresponding aggregation times.

If the bimodal HX distribution arose from two types of aggregate species made up of monomers in a different conformation, converting one aggregate species to another (e.g., small oligomers to larger condensed oligomers) by extending the aggregation time would change the ratio of two mass peaks in the bimodal HX distribution. HX analysis of three aggregate samples at different aggregation times showed two distinct features. First, all of the 8 reporter peptides from three bimodal regions had an approximate 1:1 ratio bimodal distribution in mass spectra (representative peptide 147−180 shown in Figure 7). Second, this 1:1 ratio was preserved when the aggregation time increased from 2.5 min to 5 and 15 min for all of the three bimodal regions. This is shown for reporter peptide 147−180 in Figure 9 and peptides 72−102 and 229−245 in Figure 10. These observations argue against the conversion of one conformation into another. Rather, they are more consistent with more than one molecular conformation present in one aggregate species assembled at a stoichiometry of approximately 1:1 in the aggregates. However, another possibility consistent with the HX labeling observations is two different kinds of aggregates, each made up of a different conformation, that only self-associate and do not interconvert.

Prediction of Aggregation Hot Spots by Computational Tools. A number of computational tools have been developed to predict polypeptide sequences with high self-association propensity (*36*, *37*, *60*−*62*). Though these predictive tools were developed based on different algorithms, consensus predictions from their combined use may indicate the regions that are most likely to self-associate as β-sheet and/or amyloid structures in aggregates ("hot spots"). Figure 11 shows the residues within aCgn predicted to have high propensity to self-associate by three predictive tools (TANGO (*36*), PASTA (*63*), AGGRESCAN (*61*)) that are accessible to the public as web-based servers.

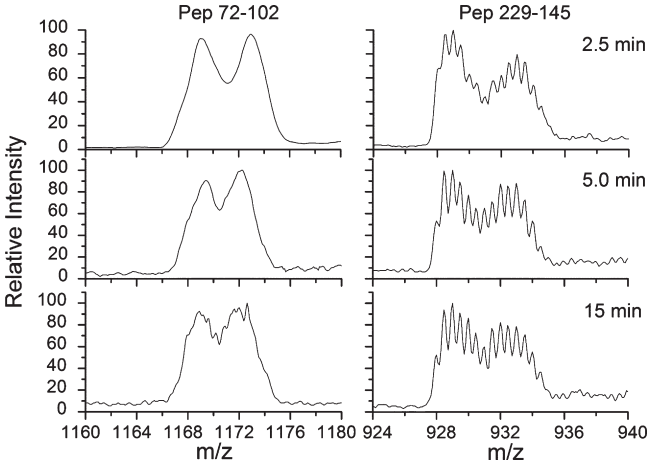

FIGURE 10: Bimodal HX distribution mass spectra obtained for reporter peptides 72−102 and 229−245 from 2.5, 5.0, and 15 min aggregation. The deuterium labeling time was 600 min for all three aggregate samples.

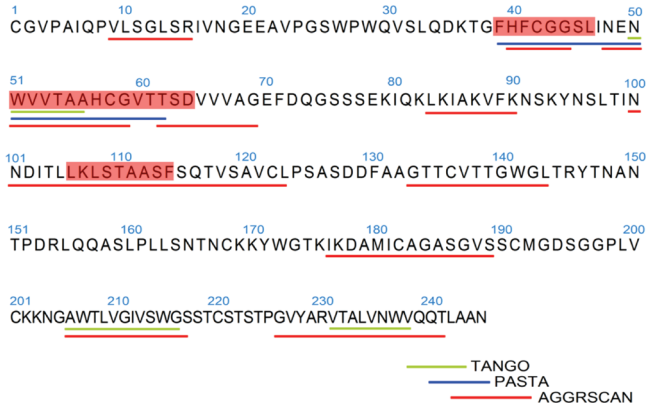

FIGURE 11: Aggregation hot spots of aCgn predicted by the three computational tools as described in the text. Regions predicted as aggregation prone by at least two algorithms are identified as consensus regions of self-association. The highlighted residues are the amyloid-forming segments suggested by peptide level HX analysis.

The regions predicted to self-associate by at least two of the three algorithms ("consensus hotspots") include residues 40−44, 48−62, 206−216, and 231−238. For comparison, the three segments (39−46, 51−64, and 106−114) suggested to be involved in the formation of β-sheet fibril core by peptide level HX are also highlighted in Figure 11. It can be seen that two out of three amyloid-forming segments identified by HX analysis were predicted as consensus aggregation hot spots, though two false positives were also predicted.

DISCUSSION

Nonnative protein aggregation is critical to a number of protein deposition diseases (*4*) and also the formulation of therapeutic proteins (*64*, *65*). A common strategy to increase protein stability against aggregation is to use a pH below the p*I* and low ionic strength, in order to enhance the repulsive interactions between protein molecules (*24*, *25*). Despite these repulsive interactions, proteins under such conditions are capable of forming large aggregates (*5*, *26*, *28*). Unfortunately, the structures of such complex aggregates are difficult to study and are poorly understood.

A major goal of this present study was to characterize the structural features of nonnative aggregates from model protein aCgn and determine if they possess amyloid characteristics. To achieve this goal, Congo red binding and X-ray diffraction were first performed. The results shown in Figure 2B,C clearly demonstrated the presence of amyloid structure in aCgn aggregates by substantially increased Congo red binding and X-ray diffraction cross-β patterns typical of amyloids. In addition, the presence of strong IR absorption at 1627 cm^{-1} and weak absorption at 1690 cm^{-1} in FT-IR spectra of both native monomer and thermally induced aggregates (Figure 3) suggested that antiparallel β-stand orientations are present in both states. For native monomer, the contribution of antiparallel β-stand orientation agrees with the aCgn crystal structure shown in Figure 8B.

Global HX analysis of the monomeric and aggregated states in Figure 4 suggested that aCgn monomers within aggregates were substantially unfolded, consistent with increased Trp exposure upon aggregation in an independent fluorescence analysis described previously (*66*). The increased solvent exposure is not unexpected, given that a temperature above the protein melting temperature was used to drive the aggregation process in this study. However, such an increased solvent accessibility upon aCgn amyloid formation is in contrast to many other amyloid-forming cases which showed significantly reduced global solvent accessibility such as for amyloid-β (*67*), α-synuclein (*34*), insulin (*68*), and β2-microglobulin (*35*). Thus, in contrast to these proteins, only a small fraction of the aCgn sequence (three blue segments and possible uncovered sequence shown in Figure 8) can possibly participate in the solvent-protected amyloid core in the aggregates.

Peptide level HX analysis provided additional details about local structural reorganization occurring during aCgn amyloid aggregation. First, as shown in Figure 8B, global structural unfolding was observed in the aggregates. This is consistent with the high incubation temperature of 65 °C, which is about 5−6 °C above the melting temperature (*39*). Second, despite the strongly destabilizing conditions, the three segments (39−46, 51−64, and 106−114) which adopt native β-sheet in monomeric state appeared to form extended β-sheets in the aggregated state. It is noteworthy other proteins have been shown to reorganize native β-sheets into cross-β amyloid (*35*, *69*, *70*). This may imply native β-strands could play a role in the formation of amyloid fibrils for β-sheet-rich proteins. However, it should be noted that native β-sheet structure is certainly not required for amyloid formation of α-helical-rich proteins such as insulin (*12*) and muscle myoglobin (*5*).

The amyloid-forming segments identified by HX showed some agreement with aggregation hot spot predictions by combined use of multiple predictive tools, providing new evidence of their potential applications to general globular proteins. Unfortunately, because each algorithm is based on its own model and assumptions regarding what the important factors are for aggregation propensity, and none of the available calculators are derived from a common set of physical laws or principles, there currently appears to be no way to conclusively determine why one algorithm performs better than another.

In addition, three bimodal regions were identified in aCgn aggregates. Similar results of bimodal HX distribution have also been observed for α-synuclein in formed amyloid fibrils and were believed to arise from heterogeneous molecule assembly in the aggregates (*34*). In the present study, a more thorough analysis of

Table 1: Number of Hydrogens Remaining Protected from Exchange Calculated for Highly Protected Reporter Peptides, 39−46, 51−64, and 106−114, and Three Bimodal Reporter Peptides, 65−97, 147−180, and 229−245

peptide group	peptide	protected hydrogens[a]	protected hydrogens[b]
protected	39−46	5.3	N/A
	51−64	11.6	N/A
	106−114	6.0	N/A
bimodal	65−97	15.6	0
	147−180	16.2	0
	229−245	5.7	0
intact aCgn	1−245	51.7	N/A

[a]The number of hydrogens remaining protected from exchange for protected and bimodal peptides and intact aCgn. In the case of bimodal peptides, the values are for the less labeled peak in Figure 7. [b]The number of hydrogens remaining protected from exchange for the more labeled peak of bimodal peptides in Figure 7. Because this peak coincides with the fully labeled control, the number of protected hydrogens is zero.

the bimodal regions was possible and could provide more structural information about these regions. It is interesting to note that peptide level HX analysis of aCgn aggregates suggested three bimodal regions that covered about one-third of the sequence (Figure 8). In contrast, intact HX mass spectra in Figure 4 lack a second mass peak at any labeling time. This discrepancy can be resolved by a quantitative analysis of deuterium incorporation into both intact molecule and reporter peptides. Intact aCgn molecule could reach a maximum deuterium labeling of 78% after 600 min; i.e., about 52 out of 235 exchangeable backbone amide protons (245 residues minus 9 Pro and the first N-terminal residue) were highly protected from deuterium labeling. At the peptide level, protected amide protons were calculated for the highly protected (39−46, 51−64, and 106−114) and bimodal (65−97, 147−180, and 229−245) reporter peptides. Values are shown in Table 1. If it is assumed that all three bimodal regions have solvent-protected structure in one molecule conformation and solvent-unprotected structure in the other, then the mass difference for these two conformations would be (15.6 + 16.2 + 5.7)/(+14 charge state) = 2.7, large enough to be resolved into two peaks for intact aCgn mass spectra in Figure 4A. Further, the total protected amide protons for the protected molecule conformation from the highly protected and bimodal regions would be (5.3 + 11.6 + 6.0) + (15.6 + 16.2 + 5.7) = 60.4. This value is significantly larger than 51.7 calculated from intact molecule analysis. The quantitative analysis suggests that no single molecular conformation contains all of the three bimodal regions in protected conformation. In other words, one molecular conformation must have solvent-protected structure in only one or two bimodal regions and unprotected structure in the other bimodal regions.

The aggregate structural information from different measurements was combined to create a hypothetical molecular model for aCgn amyloid aggregates (see Supporting Information for the details of model construction). Available structural constraints based on the experimental data include the following: (1) aCgn aggregates contain extended β-sheets as judged from the X-ray cross-β pattern; (2) HX-protected reporter peptides 39−46, 51−64, and 106−114 are strong candidates for participation in the formation of extended β-sheet core of the fibrils; (3) these extended β-sheets may be in antiparallel orientation as inferred by FT-IR; (4) to account for the HX bimodal segments (residues 65−102, 160−180, 229−245), two distinct conformations of aCgn

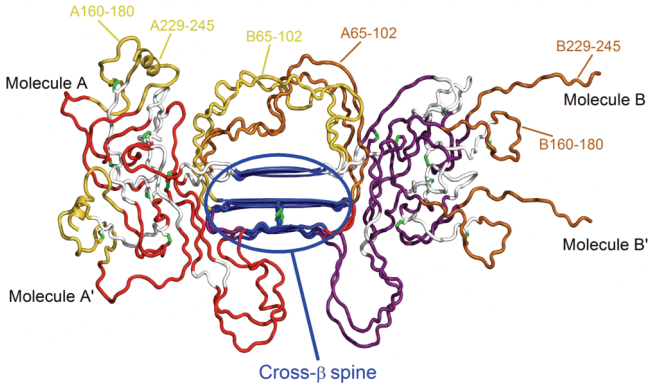

FIGURE 12: Structural model representing the hypothesized average backbone arrangement of aCgn molecules in amyloid aggregates. Three solvent-protected segments (coded blue) are arranged in antiparallel β-sheets forming amyloid spine. The segments with bimodal HDX are illustrated in two different conformations labeled as molecule A (red) and molecule B (purple) which stack along the fibril axis in an alternating mode, with yellow and orange highlighting their local structural difference in three bimodal regions. Green sticks represent the five disulfide bonds in aCgn molecule.

molecules are assembled in the amyloid aggregates at approximately 1:1 stoichiometry; (5) each conformation has solvent-protected structure in one or two bimodal regions and unprotected structure in the other bimodal regions; (6) the aCgn aggregates are formed under oxidizing conditions, and all disulfide bonds remain preserved in the aggregated state.

Using the above constraints, a molecular structural model of aCgn aggregates was built and is illustrated in Figure 12. In this structural model, the backbone of the fibrils is formed by three highly solvent-protected segments 39−46, 51−64, and 106−114 (colored blue) assembled in antiparallel β-sheets. In particular, β-sheets formed of segments 51−64 and 106−114 were modeled with 4.6 Å strand to strand distance and 9.5 Å sheet to sheet distance to match the observed reflections in the X-ray diffraction pattern shown in Figure 2C. Segment 39−46 is cross-linked to segment 51−64 by disulfide bond Cys42−Cys58 which places these at distance not larger than 7.0 Å. However, in the X-ray diffraction pattern, there is no reflection close to 7.0 Å. Thus segments 39−46 were modeled as variable in distance with respect to the middle sheet formed by segment 51−64.

As discussed in the Results, the bimodal hydrogen exchange observations could be consistent with either one type of aggregate built from two building block conformations or, alternatively, two types of aggregates each built from a different building block conformation. The amyloid core of the aggregate depicted in Figure 12 would be the same for both possibilities as described above. The three bimodal regions may adopt multiple possible arrangements of protected and unprotected regions in specific conformations. Thermally induced aCgn aggregates could be either dominated by one particular combination or comprised of a statistical distribution of all possible combinations. No experimental evidence was available in this study to distinguish these two cases. For illustration purposes in Figure 12, a specific configuration is shown in which the two bimodal regions, 160−180 and 229−245, have protected structure (coded yellow) in molecule A and unprotected structure (coded orange) in molecule B. The other bimodal region, 65−102, has unprotected structure (coded orange) in molecule A and protected structure (coded yellow) in molecule B. The model in Figure 12 includes an alternating set of monomers along the fibril axis with distinct

conformations of molecules A and B. Furthermore, because amyloid formation of aCgn was carried under oxidizing conditions, in accordance all five disulfide bonds (highlighted in green stick) were preserved in the model of aCgn aggregates. Four of the five disulfide bonds lie outside of the fibril core, and cross-link into a bulky bundle with dimensions larger than the 9.2 Å (4.6 Å × 2) repeat of the antiparallel β-strands. Thus, to fit the residues outside of the fibril core, the region 122 to C-terminus was slightly rotated and translated for both molecules A and B in Figure 12. The resulting molecules are labeled A′ and B′.

Solvent-exposed regions in aCgn aggregates identified by HX are colored red in molecules A and A′ and purple in molecules B and B′ in Figure 12. Five Trp residues out of eight in total are located in these solvent-exposed regions in the created structure model in contrast to three in aCgn native monomer (data not shown). Therefore, the model would indicate that two additional Trp residues become solvent exposed upon the formation of aCgn aggregates. This agrees well with Trp fluorescence analysis of aCgn native monomer and thermally induced aggregates in a previous study which suggested that 40−60% of the buried Trp in native monomer were exposed upon formation of the aggregates (*66*).

It has been shown that amyloid fibrils may exhibit a variety of morphologies as a result of different aggregation conditions. For instance, β_2-microglobulin has been shown to form three types of amyloid fibrils including semiflexible, long rigid, and short rod-like fibrils under three aggregation conditions (*51*, *52*). In our case, the thermally induced aCgn aggregation led to semiflexible rather than long rigid fibrils (*46*). The structural model in Figure 12 may provide a possible explanation for the semiflexible morphology. The extended β-sheets formed by three short segments would provide the strong, spatially specific interactions to promote a rigid rod-like morphology. However, the presence of significant disordered regions, as well as constraints of disulfide bonds, outside the spine may introduce larger steric barriers that would prevent long-range order in such structures, resulting in the semiflexible morphology. Unfortunately, direct comparison of aCgn molecular structure in two types of fibril morphology was not possible in the present study because long rigid aCgn amyloid fibrils have not been observed. However, it has been suggested in the cases of β_2-microglobulin (*42*) and amyloid-β protein (*71*) that the involvement of more residues into the amyloid core structure (thus less disordered regions in the fibrils) would lead to the formation of long fibrils with rigid morphology.

In summary, with X-ray fibril diffraction and Congo red binding, we demonstrated that the thermally induced aCgn aggregation at low pH and low ionic strength led to nonnative aggregates with amyloid structure. Using peptide level HX, we were able to show that a small fraction of the polypeptide sequence was involved in the amyloid core and sufficient to result in amyloid structure. The extensive amount of disordered sequence may also explain the resulting semiflexible chain morphology observed. The amyloid-forming segments identified by HX showed some agreement with aggregation hot spot predictions by combined use of multiple predictive tools, providing new evidence of their potential applications to general globular proteins.

ACKNOWLEDGMENT

We thank the staff at the Advanced Photon Source beamline 24-ID-E for their assistance in collecting the X-ray diffraction results.

SUPPORTING INFORMATION AVAILABLE

Structure model creation for aCgn amyloid fibrils. This material is available free of charge via the Internet at http://pubs.acs.org.

REFERENCES

1. Li, Y., Ogunnaike, B. A., and Roberts, C. I. (2010) Multi-variate approach to global protein aggregation behavior and kinetics: Effects of pH, NaCl, and temperature for alpha-chymotrypsinogen A. *J. Pharm. Sci. 99*, 645–662.
2. Qin, Z. J., Hu, D. M., Zhu, M., and Fink, A. L. (2007) Structural characterization of the partially folded intermediates of an immunoglobulin light chain leading to amyloid fibrillation and amorphous aggregation. *Biochemistry 46*, 3521–3531.
3. Dobson, C. M. (2003) Protein folding and misfolding. *Nature 426*, 884–890.
4. Chiti, F., and Dobson, C. M. (2006) Protein misfolding, functional amyloid, and human disease. *Annu. Rev. Biochem. 75*, 333–366.
5. Fandrich, M., Fletcher, M. A., and Dobson, C. M. (2001) Amyloid fibrils from muscle myoglobin—Even an ordinary globular protein can assume a rogue guise if conditions are right. *Nature 410*, 165–166.
6. Guijarro, J. I., Sunde, M., Jones, J. A., Campbell, I. D., and Dobson, C. M. (1998) Amyloid fibril formation by an SH3 domain. *Proc. Natl. Acad. Sci. U.S.A. 95*, 4224–4228.
7. Luhrs, T., Ritter, C., Adrian, M., Riek-Loher, D., Bohrmann, B., Doeli, H., Schubert, D., and Riek, R. (2005) 3D structure of Alzheimer's amyloid-beta(1−42) fibrils. *Proc. Natl. Acad. Sci. U.S.A. 102*, 17342–17347.
8. Petkova, A. T., Leapman, R. D., Guo, Z. H., Yau, W. M., Mattson, M. P., and Tycko, R. (2005) Self-propagating, molecular-level polymorphism in Alzheimer's beta-amyloid fibrils. *Science 307*, 262–265.
9. Serpell, L. C., Berriman, J., Jakes, R., Goedert, M., and Crowther, R. A. (2000) Fiber diffraction of synthetic alpha-synuclein filaments shows amyloid-like cross-beta conformation. *Proc. Natl. Acad. Sci. U.S.A. 97*, 4897–4902.
10. Ivanova, M. I., Sawaya, M. R., Gingery, M., Attinger, A., and Eisenberg, D. (2004) An amyloid-forming segment of beta 2-microglobulin suggests a molecular model for the fibril. *Proc. Natl. Acad. Sci. U.S.A. 101*, 10584–10589.
11. Sawaya, M. R., Sambashivan, S., Nelson, R., Ivanova, M. I., Sievers, S. A., Apostol, M. I., Thompson, M. J., Balbirnie, M., Wiltzius, J. J. W., McFarlane, H. T., Madsen, A. O., Riekel, C., and Eisenberg, D. (2007) Atomic structures of amyloid cross-beta spines reveal varied steric zippers. *Nature 447*, 453–457.
12. Jimenez, J. L., Nettleton, E. J., Bouchard, M., Robinson, C. V., Dobson, C. M., and Saibil, H. R. (2002) The protofilament structure of insulin amyloid fibrils. *Proc. Natl. Acad. Sci. U.S.A. 99*, 9196–9201.
13. Klunk, W. E., Jacob, R. F., and Mason, R. P. (1999) Quantifying amyloid beta-peptide (A beta) aggregation using the Congo red A beta (CR-A beta) spectrophotometric assay. *Anal. Biochem. 266*, 66–76.
14. Serpell, L. C. (2000) Alzheimer's amyloid fibrils: Structure and assembly. *Biochim. Biophys. Acta 1502*, 16–30.
15. Sunde, M., Serpell, L. C., Bartlam, M., Fraser, P. E., Pepys, M. B., and Blake, C. C. F. (1997) Common core structure of amyloid fibrils by synchrotron X-ray diffraction. *J. Mol. Biol. 273*, 729–739.
16. Weiss, W. F., Hodgdon, T. K., Kaler, E. W., Lenhoff, A. M., and Roberts, C. J. (2007) Nonnative protein polymers: Structure, morphology, and relation to nucleation and growth. *Biophys. J. 93*, 4392–4403.
17. Fink, A. L. (1998) Protein aggregation: Folding aggregates, inclusion bodies and amyloid. *Folding Des. 3*, R9–R23.
18. Purohit, V. S., Middaugh, C. R., and Balasubramanian, S. V. (2006) Influence of aggregation on immunogenicity of recombinant human factor VIII in hemophilia A mice. *J. Pharm. Sci. 95*, 358–371.
19. Rosenberg, A. S. (2006) Effects of protein aggregates: An immunologic perspective. *AAPS J. 8*, E501–E507.
20. Bachmann, M. F., and Zinkernagel, R. M. (1997) Neutralizing antiviral B cell responses. *Annu. Rev. Immunol. 15*, 235–270.
21. Cromwell, M. E. M., Hilario, E., and Jacobson, F. (2006) Protein aggregation and bioprocessing. *AAPS J. 8*, E572–E579.
22. Chi, E. Y., Krishnan, S., Randolph, T. W., and Carpenter, J. F. (2003) Physical stability of proteins in aqueous solution: Mechanism and driving forces in nonnative protein aggregation. *Pharm. Res. 20*, 1325–1336.

23. Shire, S. J., Shahrokh, Z., and Liu, J. (2004) Challenges in the development of high protein concentration formulations. *J. Pharm. Sci. 93*, 1390–1402.
24. Chi, E. Y., Krishnan, S., Kendrick, B. S., Chang, B. S., Carpenter, J. F., and Randolph, T. W. (2003) Roles of conformational stability and colloidal stability in the aggregation of recombinant human granulocyte colony-stimulating factor. *Protein Sci. 12*, 903–913.
25. Tsai, A. M., van Zanten, J. H., and Betenbaugh, M. J. (1998) II. Electrostatic effect in the aggregation of heat-denatured RNase A and implications for protein additive design. *Biotechnol. Bioeng. 59*, 281–285.
26. Whittingham, J. L., Scott, D. J., Chance, K., Wilson, A., Finch, J., Brange, J., and Dodson, G. G. (2002) Insulin at pH 2: Structural analysis of the conditions promoting insulin fibre formation. *J. Mol. Biol. 318*, 479–490.
27. Gosal, W. S., Clark, A. H., Pudney, P. D. A., and Ross-Murphy, S. B. (2002) Novel amyloid fibrillar networks derived from a globular protein: Beta-lactoglobulin. *Langmuir 18*, 7174–7181.
28. McCammon, M. G., Scott, D. J., Keetch, C. A., Greene, L. H., Purkey, H. E., Petrassi, H. M., Kelly, J. W., and Robinson, C. V. (2002) Screening transthyretin amyloid fibril inhibitors: Characterization of novel multiprotein, multiligand complexes by mass spectrometry. *Structure 10*, 851–863.
29. Krebs, M. R. H., Wilkins, D. K., Chung, E. W., Pitkeathly, M. C., Chamberlain, A. K., Zurdo, J., Robinson, C. V., and Dobson, C. M. (2000) Formation and seeding of amyloid fibrils from wild-type hen lysozyme and a peptide fragment from the beta-domain. *J. Mol. Biol. 300*, 541–549.
30. Sagis, L. M. C., Veerman, C., and van der Linden, E. (2004) Mesoscopic properties of semiflexible amyloid fibrils. *Langmuir 20*, 924–927.
31. Munishkina, L. A., Henriques, J., Uversky, V. N., and Fink, A. L. (2004) Role of protein-water interactions and electrostatics in alpha-synuclein fibril formation. *Biochemistry 43*, 3289–3300.
32. Krebs, M. R. H., Devlin, G. L., and Donald, A. M. (2007) Protein particulates: Another generic form of protein aggregation? *Biophys. J. 92*, 1336–1342.
33. Petkova, A. T., Ishii, Y., Balbach, J. J., Antzutkin, O. N., Leapman, R. D., Delaglio, F., and Tycko, R. (2002) A structural model for Alzheimer's beta-amyloid fibrils based on experimental constraints from solid state NMR. *Proc. Natl. Acad. Sci. U.S.A. 99*, 16742–16747.
34. Del Mar, C., Greenbaum, E. A., Mayne, L., Englander, S. W., and Woods, V. L. (2005) Structure and properties of alpha-synuclein and other amyloids determined at the amino acid level. *Proc. Natl. Acad. Sci. U.S.A. 102*, 15477–15482.
35. Hoshino, M., Katou, H., Hagihara, Y., Hasegawa, K., Naiki, H., and Goto, Y. (2002) Mapping the core of the beta(2)-microglobulin amyloid fibril by H/D exchange. *Nat. Struct. Biol. 9*, 332–336.
36. Fernandez-Escamilla, A. M., Rousseau, F., Schymkowitz, J., and Serrano, L. (2004) Prediction of sequence-dependent and mutational effects on the aggregation of peptides and proteins. *Nat. Biotechnol. 22*, 1302–1306.
37. Tartaglia, G. G., Cavalli, A., Pellarin, R., and Caflisch, A. (2005) Prediction of aggregation rate and aggregation-prone segments in polypeptide sequences. *Protein Sci. 14*, 2723–2734.
38. Zhang, A., Qi, W., Good, T. A., and Fernandez, E. J. (2009) Structural differences between A beta(1−40) intermediate oligomers and fibrils elucidated by proteolytic fragmentation and hydrogen/deuterium exchange. *Biophys. J. 96*, 1091–1104.
39. Andrews, J. M., and Roberts, C. J. (2007) Non-native aggregation of alpha-chymotrypsinogen occurs through nucleation and growth with competing nucleus sizes and negative activation energies. *Biochemistry 46*, 7558–7571.
40. Andrews, J. M., Weiss, W. F., and Roberts, C. J. (2008) Nucleation, growth, and activation energies for seeded and unseeded aggregation of alpha-chymotrypsinogen A. *Biochemistry 47*, 2397–2403.
41. Williams, A. D., Sega, M., Chen, M. L., Kheterpal, I., Geva, M., Berthelier, V., Kaleta, D. T., Cook, K. D., and Wetzel, R. (2005) Structural properties of A beta protofibrils stabilized by a small molecule. *Proc. Natl. Acad. Sci. U.S.A. 102*, 7115–7120.
42. Yamaguchi, K. I., Katou, H., Hoshino, M., Hasegawa, K., Naiki, H., and Goto, Y. (2004) Core and heterogeneity of beta(2)-microglobulin amyloid fibrils as revealed by H/D exchange. *J. Mol. Biol. 338*, 559–571.
43. Harper, J. D., Wong, S. S., Lieber, C. M., and Lansbury, P. T. (1997) Observation of metastable A beta amyloid protofibrils by atomic force microscopy. *Chem. Biol. 4*, 119–125.
44. Glabe, C. C. (2005) Amyloid accumulation and pathogensis of Alzheimer's disease: Significance of monomeric, oligomeric and fibrillar Abeta. *Subcell. Biochem. 38*, 167–177.
45. Glabe, C. G., and Kayed, R. (2006) Common structure and toxic function of amyloid oligomers implies a common mechanism of pathogenesis. *Neurology 66*, S74–S78.
46. Weiss, W. F. T., Hodgdon, T. K., Kaler, E. W., Lenhoff, A. M., and Roberts, C. J. (2007) Nonnative protein polymers: Structure, morphology, and relation to nucleation and growth. *Biophys. J. 93*, 4392–4403.
47. Jones, T. A., Zou, J. Y., Cowan, S. W., and Kjeldgaard, M. (1991) Improved methods for building protein models in electron-density maps and the location of errors in these models. *Acta Crystallogr. A 47*, 110–119.
48. Emsley, P., and Cowtan, K. (2004) Coot: Model-building tools for molecular graphics. *Acta Crystallogr. D 60*, 2126–2132.
49. Brunger, A. T., Adams, P. D., Clore, G. M., DeLano, W. L., Gros, P., Grosse-Kunstleve, R. W., Jiang, J. S., Kuszewski, J., Nilges, M., Pannu, N. S., Read, R. J., Rice, L. M., Simonson, T., and Warren, G. L. (1998) Crystallography & NMR system: A new software suite for macromolecular structure determination. *Acta Crystallogr. D 54*, 905–921.
50. Li, Y., Weiss, W. F., and Roberts, C. J. (2009) Characterization of high-molecular-weight nonnative aggregates and aggregation kinetics by size exclusion chromatography with inline multi-angle laser light scattering. *J. Pharm. Sci. 98*, 3997–4016.
51. Gosal, W. S., Morten, I. J., Hewitt, E. W., Smith, D. A., Thomson, N. H., and Radford, S. E. (2005) Competing pathways determine fibril morphology in the self-assembly of beta(2)-microglobulin into amyloid. *J. Mol. Biol. 351*, 850–864.
52. Kad, N. M., Myers, S. L., Smith, D. P., Smith, D. A., Radford, S. E., and Thomson, N. H. (2003) Hierarchical assembly of beta(2)-microglobulin amyloid in vitro revealed by atomic force microscopy. *J. Mol. Biol. 330*, 785–797.
53. Stathopulos, P. B., Scholz, G. A., Hwang, Y. M., Rumfeldt, J. A. O., Lepock, J. R., and Meiering, E. M. (2004) Sonication of proteins causes formation of aggregates that resemble amyloid. *Protein Sci. 13*, 3017–3027.
54. Cooper, J. H. (1969) An evaluation of current methods for the diagnostic histochemistry of amyloid. *J. Clin. Pathol. 22*, 410–413.
55. Conway, K. A., Harper, J. D., and Lansbury, P. T. (2000) Fibrils formed in vitro from alpha-synuclein and two mutant forms linked to Parkinson's disease are typical amyloid. *Biochemistry 39*, 2552–2563.
56. Bouchard, M., Zurdo, J., Nettleton, E. J., Dobson, C. M., and Robinson, C. V. (2000) Formation of insulin amyloid fibrils followed by FTIR simultaneously with CD and electron microscopy. *Protein Sci. 9*, 1960–1967.
57. Hvidt, A., and Nielsen, S. O. (1966) Hydrogen exchange in proteins. *Adv. Protein Chem. 21*, 287–386.
58. Cierpicki, T., Bielnicki, J., Zheng, M. Y., Gruszczyk, J., Kasterka, M., Petoukhov, M., Zhang, A., Fernandez, E. J., Svergun, D. I., Derewenda, U., Bushweller, J. H., and Derewenda, Z. S. (2009) The solution structure and dynamics of the DH-PH module of PDZRhoGEF in isolation and in complex with nucleotide-free RhoA. *Protein Sci. 18*, 2067–2079.
59. Wang, D. C., Bode, W., and Huber, R. (1985) Bovine chymotrypsinogen-a X-ray crystal-structure analysis and refinement of a new crystal form at 1.8 Å resolution. *J. Mol. Biol. 185*, 595–624.
60. Pawar, A. P., DuBay, K. F., Zurdo, J., Chiti, F., Vendruscolo, M., and Dobson, C. M. (2005) Prediction of "aggregation-prone" and "aggregation-susceptible" regions in proteins associated with neurodegenerative diseases. *J. Mol. Biol. 350*, 379–392.
61. Conchillo-Sole, O., de Groot, N. S., Aviles, F. X., Vendrell, J., Daura, X., and Ventura, S. (2007) AGGRESCAN: A server for the prediction and evaluation of "hot spots" of aggregation in polypeptides. *BMC Bioinf. 8*, article no. 65.
62. Trovato, A., Chiti, F., Maritan, A., and Seno, F. (2006) Insight into the structure of amyloid fibrils from the analysis of globular proteins. *PLoS Comput. Biol. 2*, e170.
63. Trovato, A., Chiti, F., Maritan, A., and Seno, F. (2006) Insight into the structure of amyloid fibrils from the analysis of globular proteins. *Plos Comput. Biol. 2*, 1608–1618.
64. Wang, W. (2005) Protein aggregation and its inhibition in biopharmaceutics. *Int. J. Pharm. 289*, 1–30.
65. Shire, S. J. (2009) Formulation and manufacturability of biologics. *Curr. Opin. Biotechnol. 20*, 708–714.

66. Weiss, W. F. (2009) Nonnative aggregation of alpha-chymotrypsinogen A and related systems, Ph.D. Dissertation, University of Delaware.
67. Qi, W., Zhang, A., Patel, D., Lee, S., Harrington, J. L., Zhao, L. M., Schaefer, D., Good, T. A., and Fernandez, E. J. (2008) Simultaneous monitoring of peptide aggregate distributions, structure, and kinetics using amide hydrogen exchange: Application to A beta(1−40) fibrillogenesis. *Biotechnol. Bioeng. 100*, 1214–1227.
68. Dzwolak, W., Smirnovas, V., Jansen, R., and Winter, R. (2004) Insulin forms amyloid in a strain-dependent manner: An FT-IR spectroscopic study. *Protein Sci. 13*, 1927–1932.
69. McParland, V. J., Kalverda, A. P., Homans, S. W., and Radford, S. E. (2002) Structural properties of an amyloid precursor of beta(2)-microglobulin. *Nat. Struct. Biol. 9*, 326–331.
70. Liu, K., Cho, H. S., Lashuel, H. A., Kelly, J. W., and Wemmer, D. E. (2000) A glimpse of a possible amyloidogenic intermediate of transthyretin. *Nat. Struct. Biol. 7*, 754–757.
71. Kheterpal, I., Chen, M., Cook, K. D., and Wetzel, R. (2006) Structural differences in A beta amyloid protofibrils and fibrils mapped by hydrogen exchange—Mass spectrometry with on-line proteolytic fragmentation. *J. Mol. Biol. 361*, 785–795.